Measuring the Accuracy of MARSS—An Airborne Microwave Radiometer

ANDREW MCGRATH AND TIM HEWISON

Met Office, Farnborough, Hampshire, United Kingdom

ABSTRACT

An airborne microwave radiometer has been thoroughly characterized by the Met Office, using a thermal-vacuum test facility and flight test data. Scan dependence due to mirror reflectivity considerations, as well as calibration target thermometry, target thermal gradients, radiometer noise, and radiometer stability are quantified. A resultant accuracy of approximately 1 K is achieved.

1. Introduction

The Microwave Airborne Radiometer Scanning System (MARSS) was originally developed as a two-channel (89 and 157 GHz) radiometer by the Met Office (United Kingdom) and Laboratoire de Météorologie Dynamique du Centre Nationale de Recherche Scientifique (France). It has been operated since 1989 on the Meteorological Research Flight C-130 aircraft. MARSS has been used to validate radiative transfer models in clear air (English et al. 1994), liquid water cloud. (English 1995), and precipitation (Jones 1995). It has also been used for characterization of the surface emissivities of sea surface (Guillou et al. 1996), sea ice and snow (Hewison and English 1999), and land surfaces (Hewison 2001; Morland et al. 2000). Although MARSS was well characterized in this form (Jones 1995), it should be noted that different applications have different calibration accuracy requirements.

In 1999, MARSS was upgraded by Rutherford Appleton Laboratories (United Kingdom) and the Met Office to include three additional channels, centered on the 183-GHz water vapor line. These new channels match those of the Advanced Microwave Sounding Unit (AMSU-B), operated on the National Oceanic and Atmospheric Administration polar orbiting satellites. Greater atmospheric absorption experienced at these wavelengths complicates the calibration method employed before the upgrade, which used views of the cosmic microwave background as a reference at high altitude. This has caused us to reexamine the calibration accuracy of MARSS, including analysis of data taken in flight and during tests in a radiometric characterization facility.

2. System description

More thoroughly described in Jones (1995), MARSS consists of a multichannel superheterodyne receiver mounted inside the aircraft fuselage, coupled onto a common optical axis, viewing a rotating scan mirror mounted in an external pod. Figure 1 shows the general arrangement. The pod also contains two blackbody calibration targets maintained at different temperatures in order to continually monitor the gain and offset of each channel. A 3-s scan period presents 20 views to the radiometer: nine upward, nine downward, and one of each of the calibration targets. Each view is held and integrated for 100 ms. The calibration targets and the measured environment are viewed directly, with no windows or other components between the observations and the scan mirror. Channels are numbered in accordance with AMSU terminology from channel 16 to 20, and the channel parameters are summarized in Table 1.

The airborne environment is a demanding one for any instrumentation. Pressure variation is not expected to have any effect on any of the MARSS components, however the temperature can vary by several kelvins on timescales of tens of minutes, even inside the C130 fuselage. Most of the receiver components have substantial temperature dependencies; the most sensitive of these are the intermediate frequency (IF) amplifiers, which incorporate active thermal control. With the receiver's large thermal mass the heat flow is complex and a substantial time is required to reach thermal equilibrium. Immediately before each takeoff, the instrument loses power when the aircraft is switched from ground power to its own engine-driven system. Outside the fuselage, the calibration targets, and scan mirror ex-

Corresponding author address: Dr. Andrew McGrath, Met Office, Bldg. Y70, Cody Technology Park, Ively Road, Farnborough, Hampshire GU14 0LX, United Kingdom.
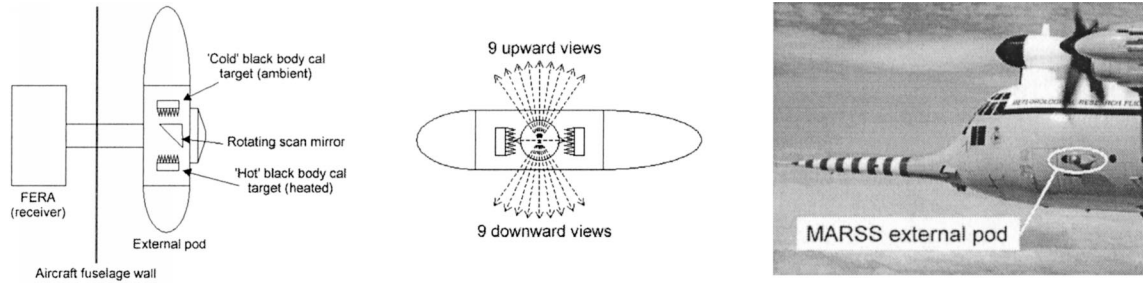E-mail: andrew.mcgrath@metoffice.com

FIG. 1. General arrangement of the MARSS radiometer. The receiver is mounted inside the fuselage, viewing the rotating scan mirror through the pylon that supports an external pod. The pod also supports two calibration targets.

perience even greater environmental fluctuations, with airflow past the pod that varies with airspeed and angle of attack, temperatures that vary as much as 100 K, and the possibility of condensation or ice formation.

Each channel is assumed to have linear response to observed brightness temperature, with a gain G and an offset T_{REC}, that may vary slowly over time, largely due to the thermal effects just mentioned. Accordingly, the brightness temperature of a scene is recovered from observations of the two calibration targets, using

$$T_B = \frac{C_B}{G} + T_{REC}, \qquad (1)$$

where T_B is the retrieved scene brightness temperature; C_B the radiometer output for view of scene; and G the channel gain, given by the ratio of the difference in radiometer output between the two calibration targets and the difference in the physical temperatures of the targets

$$G = \frac{(C_H - C_C)}{(T_h - T_c)} \qquad (2)$$

and T_{REC} = input receiver noise temperature given by

$$T_{REC} = T_c - \frac{C_C}{G}. \qquad (3)$$

3. Potential sources of error

Many factors introduce errors to brightness temperatures retrieved using Eq. (1) with a MARSS-like instrument. Some mechanisms can be accounted for with a theoretical consideration and derivation of correction terms, while others require empirical characterization.

This section identifies major sources of error that may be present in MARSS and need to be measured or checked for in a system characterization, and it also refers the reader to relevant sections of this paper. Figure 2 identifies the error sources considered. Variation of mirror reflectivity with incident polarisation angle introduces a scan dependence of as much as 1 K, discussed in more detail in section 5a.

Errors in measurement of the temperatures of the two calibration targets propagate directly into retrieved brightness temperatures through Eqs. (2) and (3). These errors arise not only from the accuracy of the platinum resistance thermometer (PRT) temperature sensors embedded in the targets, but also from the relationship between the temperatures sensed by those PRTs and the radiometric temperature of that part of the face of the targets viewed by the radiometer. Thermal gradients across and through the target substrates, and through the microwave absorbent coating, require corrections to be applied to the temperatures measured by the PRTs. PRT noise introduces random errors, which may be dealt with by careful averaging techniques, as do subfootprint-scale temperature fluctuations that may be introduced by turbulence in the air flowing past the targets. Contamination of a target view with other components, perhaps due to beam misalignment, will also lead to errors in the radiometer's views of the target, which may or may not be possible to quantify. Sections 5b,c discuss the characterization of MARSS target thermometry.

Errors will also arise if the channel responses are not linear. Nonlinearity could potentially arise due to gain compression if too much IF power is applied to the detector. Errors in target temperature (e.g., due to target view contamination by physical misalignment, antenna sidelobes, or radio interference within the receiver) would also appear as a nonlinearity in observations de-

TABLE 1. Summary of MARSS channel parameters. [Channel 16 IF bandwidth has recently been changed to 0.75–1.40 GHz.] FWHM = full-width half-maximum.

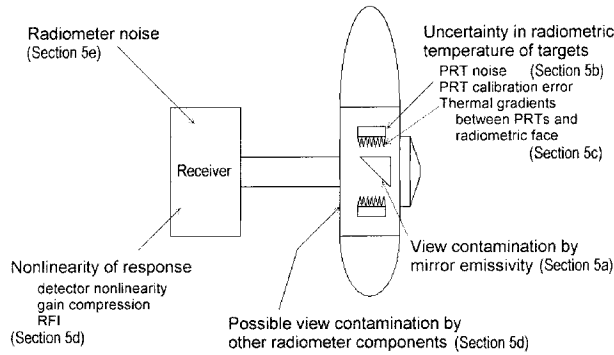| Channel	16	17	18	19	20
Center Frequency (GHz)	88.992	157.075	183.248	183.248	183.248
IF bandwidth (GHz)	1.3–3.9*	1.3–3.9	0.75–1.2	2.5–3.5	6.0–8.0
Beamwidth (FWHM)	11.8°	11.0°	6.2°	6.2°	6.2°

FIG. 2. Sources of errors in the MARSS radiometer. Each of these contributors results in an error that propagates through the radiometer equation to produce an uncertainty in retrieved brightness temperature, as discussed in the sections indicated.
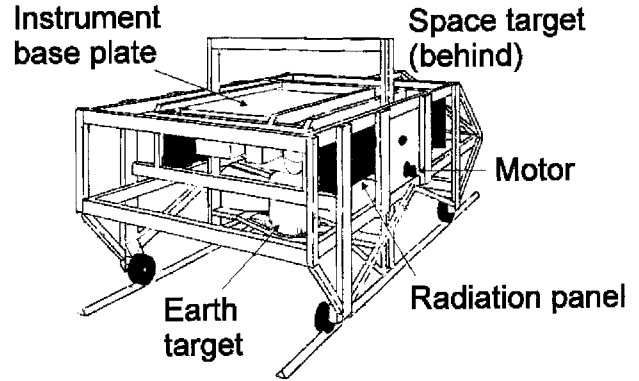

FIG. 3. Met Office test rig, used for operation and calibration of microwave radiometers in the thermal vacuum chamber. Artwork by S. Stringer.

signed to measure linearity, as discussed in section 5d. Radiometer noise is a random error contributor with components on various timescales. Section 5e discusses measurements of the radiometer stability.

4. Calibration facility

The Defence Evaluation and Research Agency at Farnborough, United Kingdom, operates a thermal-vacuum test facility extensively used by the Met Office for the calibration of satellite instruments such as AMSU-B (Saunders et al. 1995). The Met Office has a test rig, shown in Fig. 3, that allows the instrument to be mounted in the thermal vacuum chamber viewing calibration targets cooled to controlled temperatures with liquid nitrogen. One of these two calibration targets (known as the "earth target") may be controlled to temperatures between 90 and 330 K and is mounted on a swinging arm to enable view dependency testing. Radiation panels controllable from 90 to 390 K are mounted alongside the instrument for temperature control. The chamber shroud is also controllable in temperature from 233 to 343 K. A mounting frame was constructed to allow MARSS to be mounted in this rig, so that the rig's earth target may be moved into any of MARSS's downward views (normally left in the nadir position).

For satellite instrument testing, the chamber can achieve pressures of 10^{-6} hPa, but because MARSS is an aircraft instrument not designed for vacuum operation, most of the MARSS chamber tests were undertaken at pressures near 300 hPa in an atmosphere of dry nitrogen gas. However, this pressure was later increased to test its influence on MARSS's calibration.

5. Characterization of error corrections

a. Scan dependence

1) THEORY

MARSS's receiver views the blackbody calibration targets and the observed scenes via a rotating scan mir-

ror. Thermal emission by the mirror contributes to contamination of observed brightnesses due to finite reflectivity. The reflectivity of a mirror for linearly polarized radiation depends on the incident polarization angle and, accordingly, the contamination introduced by MARSS's scan mirror varies with scan position.

Thermal emission by the mirror biases each view by

$$\Delta T_B(\theta) = [1 - \Gamma(\theta)](T_{\text{mir}} - T_B), \qquad (4)$$

where T_B is brightness temperature of the scene "before" reflection; T_{mir} the temperature of the mirror; and Γ the mirror reflectivity, which varies as a function of the angle of incident polarization θ as

$$\Gamma(\theta) = \Gamma_{//} \cos^2(\theta) + \Gamma_{\perp} \sin^2(\theta). \qquad (5)$$

Here, $\Gamma_{//}$ and $\Gamma_{\perp}$ are the power reflectivities of the mirror for parallel and perpendicularly polarized radiation, which are constant for a given wavelength and plane mirror set at a constant inclination. MARSS's mirror is of stainless steel, inclined at 45°, and tabulated material property data allow us to calculate these reflectivities for the frequencies of the MARSS channels as shown in Table 2.

Figure 4 shows the effects of this scan-dependent bias on MARSS's upward views during high-level flight. The panels show the bias measured in different view positions for each channel, with respect to tip curves, based on the zenith views. The curves show the theoretical bias after the effects of the changing mirror reflectivity have been propagated through the radiometer [Eq. (1)]. Bias varies by approximately 1 K, although channel 16 shows a different trend due to different polarization

TABLE 2. Power reflectivities of a stainless steel mirror inclined at 45° for parallel and perpendicular plane polarized radiation at the MARSS channel frequencies. Bulk conductivity of stainless steel assumed to be $8 \times 10^6 \ \Omega^{-1} \ \text{m}^{-1}$.

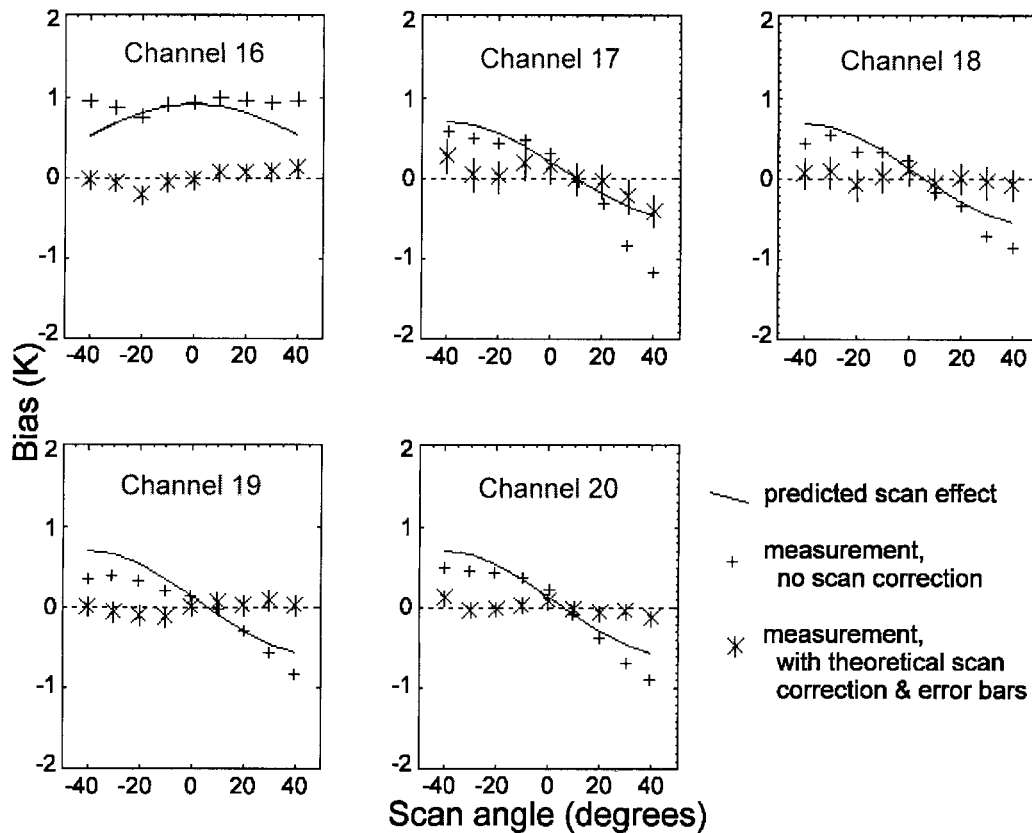| Channel	16	17	18–20
$\Gamma_{//}$	0.9934	0.9912	0.9906
$\Gamma_{\perp}$	0.9967	0.9956	0.9953

FIG. 4. Predicted and measured scan-dependent bias due to mirror reflectivity variation for MARSS's upward views at high altitude.

alignment. It can be seen that theory provides a reasonable fit to the observed bias measured in the uncorrected data, and that application of a correction based on theory substantially reduces the bias.

2) IMPLEMENTATION IN PROCESSING SYSTEM

In order to take account of the scan-dependent reflectivity effect when processing MARSS data, a correction in radiometer counts is derived and applied to all data before applying the basic radiometer equation (1) to retrieve brightness temperatures. From Eq. (4), this correction is given by multiplying the mirror's emissivity by the difference between the scene and the mirror temperature. The emissivity may be calculated from theory, using the mirror position, corresponding polarization, and reflectivity values from Table 2. Working in units of radiometer counts, the temperature of the scene is taken directly as the uncorrected radiometer output for the scene views (this approximation introduces negligible error because the mirror emissivity is low, less than 1%). Again, because of the low emissivity of the mirror, use of uncorrected target views introduces negligible error.

3) HIGH-ALTITUDE TIPPING CURVE VALIDATION

The magnitude of the bias is proportional to the difference between the temperatures of the observed scene and that of the mirror, and so it is expected to be most significant when viewing scenes of very low brightness temperatures. An experiment was performed to confirm that this scan dependence is as predicted, and that no other scan-dependent effects are present. Upward views from high-altitude flights allow observations with brightness temperatures below 10 K for all channels. The data shown in Fig. 4 are from flights at high altitude over the Baltic Sea on 5 December 1999, and on 31 August 2000 from the Cape Verde Islands to Ascension Island over the tropical Atlantic Ocean.

A tipping curve calculation (Han and Westwater 2000) is used to calculate the instrument bias for each of the upward view positions. A period of flight was chosen when a simple secant function is likely to be a good approximation for the tipping curve seen for those views (high altitude, steady flight, and optically thin atmosphere above). Averaged observations in each view position were fitted to a secant function, shown in Fig. 4 as a bias of the retrieved brightness temperature against view position. Two sets of results are shown,

one calculated without applying the scan-dependent reflectivity correction and one making the correction. It can be clearly seen that the uncorrected data show good agreement with the predicted theoretical curve shape, with the exception of channel 16. At this time, channel 16 was suffering from an interference problem, as discussed in section 5d. Application of the correction appears to leave no substantial residual view dependence for the other channels.

These results show that MARSS is not subject to scan dependence beyond the expected variation due to mirror reflectivity effects, but that the expected effects do need to be taken into account. There is some uncertainty in the value of reflectivity used (Table 2), and an analysis of these results indicates the effect of this uncertainty is a residual error of 0.27 K due to this mirror reflectivity effect.

b. Target thermometry

1) TARGET DESCRIPTION

MARSS uses two blackbody calibration targets, one of which remains at ambient temperature (known as the "ambient target") and the other of which is heated, typically to about 65°C (the "hot target"). These targets take the form of an array of pyramids, 40 mm high with bases 10 mm wide. They are constructed from a spark-eroded aluminium alloy substrate covered in a 1-mm layer Eccosorb CR114 microwave absorber. A 20-W heater is secured to the back face of the substrate of the hot target, controlled with the system operating software to maintain the selected hot target temperature. Equations (2) and (3) show the importance of accurate knowledge of the radiometric temperature of the targets. Errors in the target temperatures are propagated into the radiometer calibration. Extrapolation to low brightness temperatures results in retrieval errors three to five times greater than the target temperature errors, for temperatures typically encountered in flight.

In order to monitor the temperature of the targets, 10 PRT temperature sensors are embedded in the substrate of each. These are distributed at various positions and various depths throughout the target, to provide information about the temperature distribution through the target. In particular, one of the PRTs is mounted inside one of the target pyramids, near the tip and close to the absorber surface, as shown in Fig. 5.

2) LABORATORY CALIBRATION AGAINST REFERENCE

As part of the system characterization more thoroughly described by McGrath (2000), the PRTs in the targets were calibrated in the laboratory by attaching traceable precision reference PRTs to both the back face and the front radiometric face of each target. The targets were installed in their usual mountings in MARSS's pod and the entire pod was taken to a range of temperatures
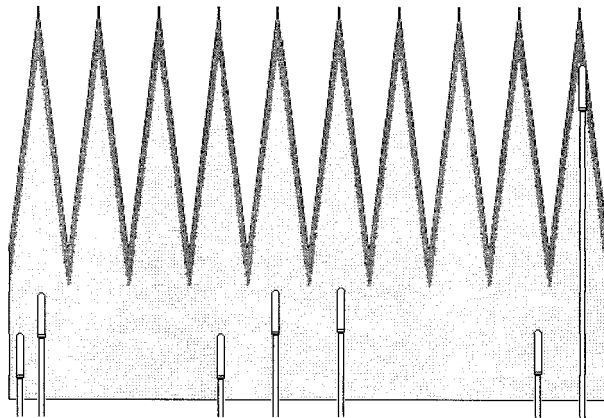

FIG. 5. Cross section of blackbody target used as calibration target for continual monitoring of MARSS's calibration parameters. Ten PRT temperature sensors are embedded in each target at various positions and depths to monitor the temperature distribution across and through the target.

between 253 and 303 K. Each temperature was held steady for several hours, to ensure thermal equilibrium was reached, while the MARSS system logged the readings of the target PRTs and an external system logged the reference PRTs. Responses were found to be uniformly linear, and offsets applied to individual sensors of between 0 and 1 K resulted in calibration of the individual target PRTs to an accuracy of approximately 50 mK. In laboratory conditions and without heating the hot target, the target temperatures are very uniform, however when the hot target is heated, and particularly in flight, the PRTs can show substantial thermal gradients through and across the targets.

For use of the targets for operational calibration of the MARSS radiometer, a weighted average of the substrate PRTs is formed to obtain a value for the physical temperature of the substrate. Weights are allocated by PRT location according to target footprint sensitivity, assuming a Gaussian footprint. At this stage of processing, the temperature recorded by the tip-mounted PRT is not used, being regarded not as part of the substrate but rather as an indicator of the magnitude of thermal gradients through the target depth.

Examination of PRT data for both targets, collected under a wide range of flight and laboratory conditions, shows that the spread of temperatures sensed by the PRTs in the hot target is typically on the order of 1 K, but that of the ambient target is generally much less than 200 mK. Extrapolation via Eqs. (1)–(3) of a 50-mK average substrate temperature uncertainty from typical target temperatures to a scene temperature of 3 K yields a resultant uncertainty of 0.26 K.

c. Target radiance

Retrieval of brightness temperatures using Eq. (1) requires knowledge of the radiometric temperatures of
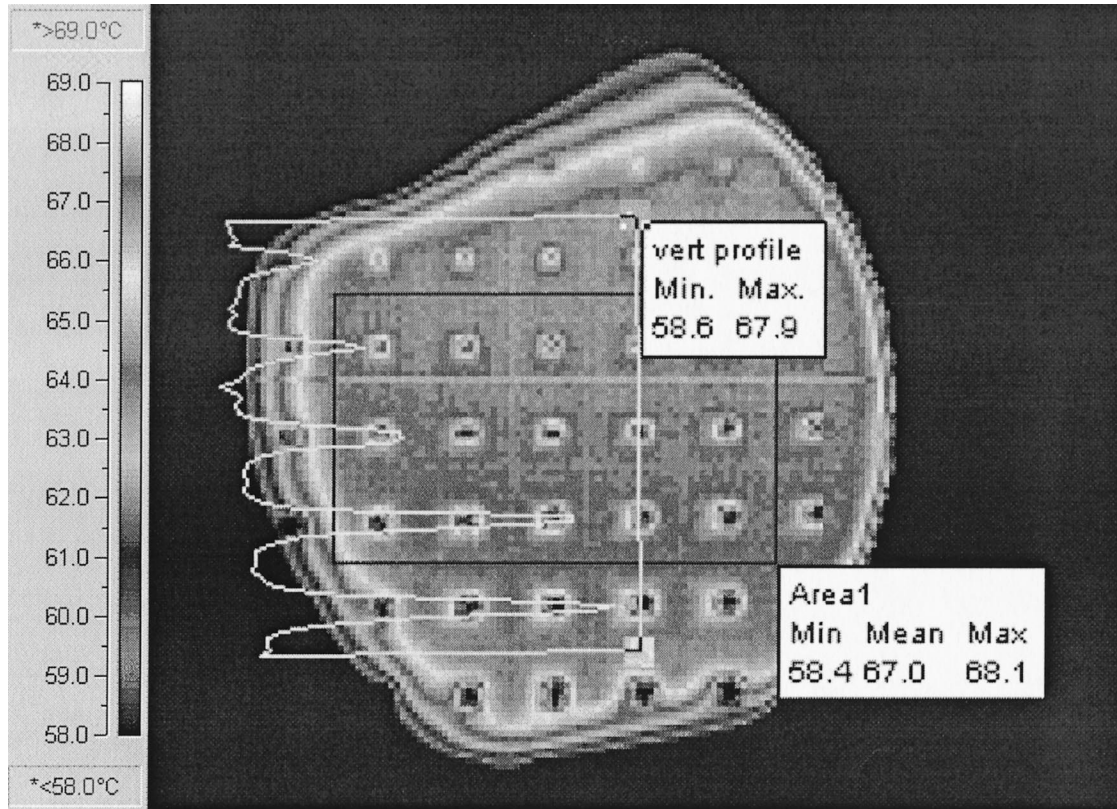
FIG. 6. Typical thermal image of heated target in situ in MARSS pod shows pyramid tips cooler than their bases, and a vertical thermal gradient due to convective currents.

the targets, as the radiometer responds to the spatially averaged radiometer temperature. This may vary from channel to channel due to differing radiometric footprints or other reasons. The reflectivity of the targets has been measured as lower than 0.0001 at MARSS frequencies (Hewison 1991). However, the temperature of the substrate, measured by the embedded PRTs, is not in general representative of the temperature of the radiometric surface of the target, due primarily to thermal gradients between the radiometric surface and the PRTs embedded in the substrate. Such gradients are usually very small in the case of the ambient target but large in the case of the hot target because of the greater contrast with the air temperature.

An infrared thermal imaging camera was used to investigate thermal gradients across the heated target. Thermographs showed the expected result that the pyramid tips are substantially cooler than the bases, and showed a thermal gradient from the bottom to the top of the vertically mounted target. A typical image is shown in Fig. 6. The vertical gradient is presumed to be due to convective currents and largely disappears when airflow is forced over the face of the target, much as would be experienced in flight.

If a suitable external radiometric reference is available, Eqs. (1)–(3) can be applied with the external ref-

erence and the ambient target to use the MARSS radiometer to retrieve the brightness temperature of the hot target. Three such external references have been used to retrieve the hot target temperature in a range of conditions. These data are then used to derive a correction to be applied to the measured target substrate temperature. Since one of the PRTs in the target is mounted near the tip of one of the target pyramids, the approach taken is to derive a correction based on the difference between the weighted PRT average giving the substrate temperature, and the temperature measured by the "tip PRT."

The earth target at 100 K was used during radiometric characterization on the calibration rig. This was used with the ambient calibration target to retrieve the hot target brightness temperature. Values obtained were very close to the hot target substrate temperature in this very stable thermal environment (i.e., small corrections ~0.1 K).

Similarly, a cryogenic target was mounted just below the MARSS pod during preflight. This comprises a box of expanded polystyrene foam, lined with foil-backed microwave absorbing foam and filled with liquid nitrogen. The boiling point of nitrogen is a simple function of atmospheric pressure, but allowance must be made for the reflection of the ambient scene in the surface of
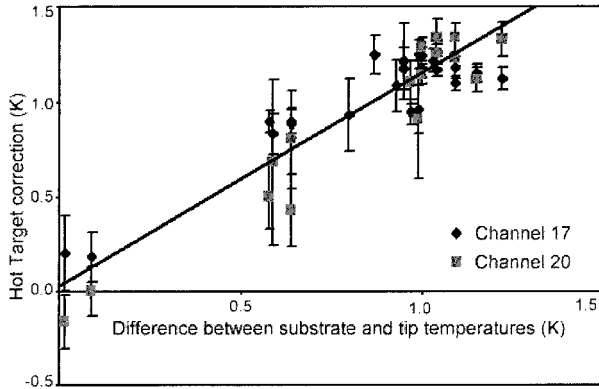
Fig. 7. Relationship between hot target correction derived from external radiometeric references, and the difference between substrate temperature and the tip PRT. Linear correlation allows estimation of required hot target correction from the measured substrate-to-tip temperature difference.

the cryogen. Vinogradov et al. (1967) measured the refractive index of liquid nitrogen at $\lambda = 2.3$ mm to be $n = 1.196 \pm 0.007$. At ambient temperatures of 290 K, this increases the apparent brightness temperature of a liquid nitrogen surface to 79.05 K. As emission is taking place near the surface of the absorber submerged in the nitrogen, allowance should be made for hydrostatic pressure due to 5-cm head of liquid nitrogen. However, this allowance amounts to 0.05 K and can be neglected. Although less stable than the earth target in the chamber, this target also resulted in very small corrections (<0.1 K) to the hot target temperature. However, both these references use measurements in still air. The gradients through the hot target's absorber coating are expected to increase in flight, with turbulent airflow around the target.

At high altitudes, atmospheric absorption above the aircraft becomes small, and its contribution can be modeled to an accuracy of better than 1 K. For MARSS, this is dominated by water vapor, which is typically measured by radiosondes to an accuracy of $\pm 15\%$ at high altitudes, where the humidity is low (Ström et al. 1994). Differences between radiative transfer models typically amount to 0.7 K for brightness temperatures of $T_B = 11$ K. This may be combined with the profile measurement accuracy to estimate the typical uncertainty of <1.0 K for modeled reference brightness temperatures below this limit.

Data from high-level runs were analyzed with respect to modeled brightness temperatures, based on collocated radiosondes. Data were only used where the radiometer was thermally stable, the aircraft was in straight, and level flight and model brightness temperatures were less than 10 K. Hot target corrections derived from channels 17 and 20 were averaged for each run and were found to range from 0.7 to 1.3 K, with typical uncertainties of 0.1 K.

Figure 7 shows the corrections derived from the high-

level runs, liquid nitrogen calibrations, and earth target chamber measurements. A strong correlation ($r^2 = 0.91$) exists between the hot target correction derived in this way and the difference measured between the PRTs in the target's base and tip. This validates the approach of using the PRT-derived substrate-to-tip gradient to estimate a target correction. A correction to estimate the brightness temperature of the hot target, ΔT_h, can be derived using the thermal gradient measured by these PRTs in the form

$$\Delta T_h = 1.12(T_{\text{base}} - T_{\text{tip}}) + 0.03. \tag{6}$$

Linear regression of the measured tip–base difference and the derived hot target correction also provides an estimate of the standard error of this correction of 0.20 K. This represents the uncertainty in our knowledge of the hot target's brightness temperature, which in turn limits the error budget of the whole calibration system. An uncertainty here of 0.20 K equates to an uncertainty of 0.65 K when typical target temperatures are used for measurement of scenes of 3-K brightness.

d. Linearity

The radiometer equations (1)–(3) are based on an assumption of linear detector response. Any nonlinearity present will result in errors in retrieved brightness temperatures, increasing for observed scenes of brightness farther from the calibration target temperatures. If a quadratic detector response is assumed, it may be shown that brightness temperatures retrieved using Eqs. (1)–(3) incur errors proportional to the product of the differences between the scene and each of the targets, with a constant of proportionality equal to that of the quadratic term in the assumed detector response.

Tests to measure the absolute accuracy of the MARSS radiometer system were undertaken in the thermal vacuum test facility. This involved maintaining a steady environment for the instrument in the chamber and varying the temperature of the calibration rig's earth target over a range of 90–330 K. Figure 8 shows the results of this test, where the difference between the earth target temperature and MARSS's radiometric measurements of it are plotted against the earth target temperature for each channel. For channels 17–20, these results show an accuracy of better than 1 K across the measurement range. Accuracy is somewhat worse at lower observed temperatures, which is expected as the measurements are extrapolated farther from the internal calibration targets. The difference between correction for a nonlinearity of this quadratic form and a linear correction similar to that introduced for target gradients also amounts to less than 1 K across the expected measurement range. Bias introduced by uncertainties in the hot target radiance (previously discussed in section 5c) is of similar magnitude and the tests performed here cannot distinguish the effects. For this reason, no separate nonline-
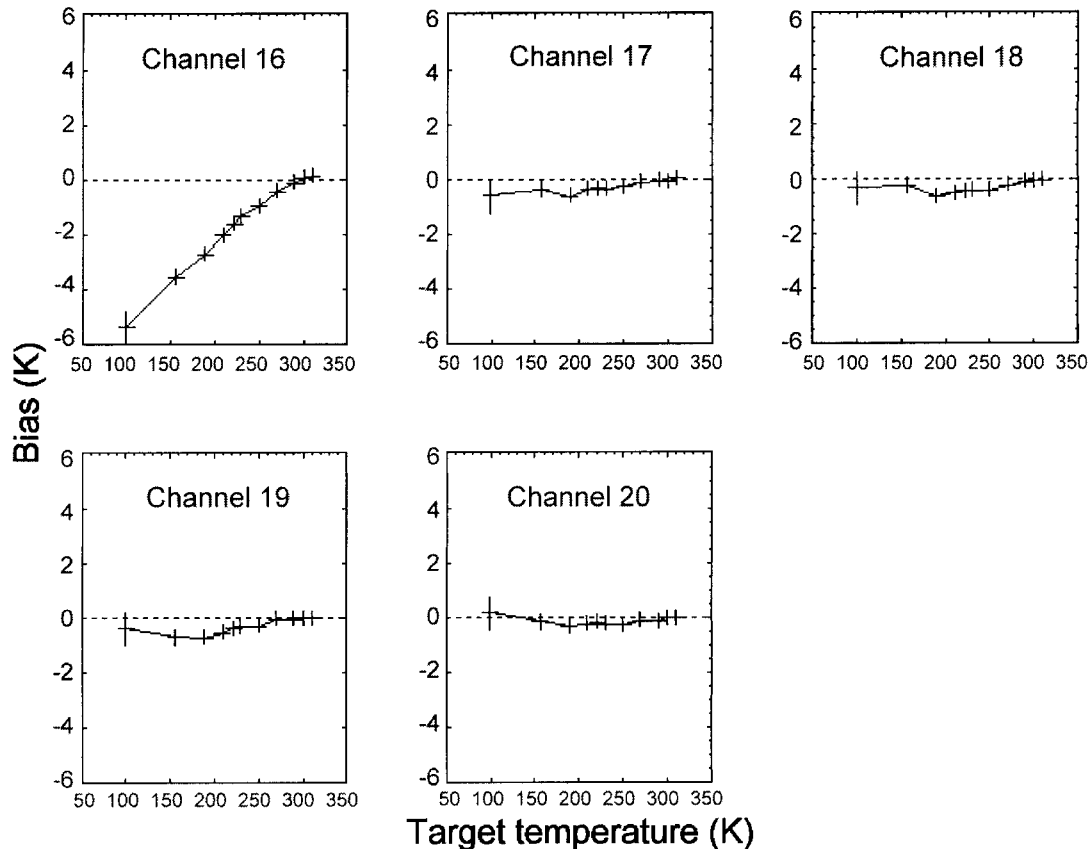
FIG. 8. Linearity–absolute accuracy results from chamber tests. The difference between the calibration rig's earth target temperature and that observed by each of MARSS's channels is plotted against the earth target temperature. Channels 17–20 show good linearity, with accuracy of better than 1 K across the measured range. Channel 16 shows a clear nonlinearity, attributed to interference.

arity correction is applied in brightness temperature retrievals.

Channel 16 shows a nonlinearity, subsequently identified as due to radio frequency interference (RFI). This nonlinearity had not been observed in operation of the instrument prior to the 1999 upgrade and is due to interference from the local oscillator introduced for the new channels. The new channels all have a center frequency of 183.248 GHz, as shown in Table 1. This is implemented using a local oscillator at half this frequency, 91.624 GHz. At the time of the upgrade it was not noticed that such a signal would beat with the 88.992-GHz channel 16 local oscillator to give a component near 2.6 GHz, central to the channel-16 IF passband. This makes channel 16 extremely sensitive to very small amounts of leakage from the new local oscillator (LO). It appears that some of the 91.6-GHz signal is emitted from the receiver and scattered from the scan mechanism in a manner that is critically dependent on the scan geometry. This scan-dependent contamination results in the observed nonlinearity. The magnitude of the nonlinearity changes substantially with tiny geom-

etry changes, such as are experienced during normal inflight operation of the instrument.

Since this design error was discovered, the problem has been eliminated by changing the IF bandpass filters in channel 16 to exclude the 2.6-GHz interference signal. The new IF bandwidth is 0.5 to 1.65 GHz, more closely matching channel 16 of AMSU-B. Tests following the modification appear to verify elimination of the interference and its consequent effects on the linearity of channel 16. Expectations are that channel 16's performance following this corrective action is now comparable with the other channels.

e. Radiometer stability

The noise spectrum of the output of a total power radiometer includes contributions from two sources. White noise from the mixer and IF amplifiers spans the measurement spectrum. This dominates the radiometric resolution ΔT_N, shown in Table 3, which is calculated from plots of standard error of views of the calibration targets, averaged over several hours of flight data. Ra-

TABLE 3. Radiometer noise measured inflight for all channels (ΔT_N). The averaging period for minimum standard error is also shown, and the averaging periods selected as the default values for processing. Channel 16 "old" and "new" refer to the values before and after change of the IF bandwidth.

Channel	ΔT_N	Averaging period for min std error(s)
16 (old)	0.23 K	26
16 (new)	0.42 K	35
17	0.69 K	32
18	0.64 K	44
19	0.44 K	37
20	0.35 K	32

FIG. 9. Typical standard error plot of radiometer output for determining optimum averaging time to minimize uncertainty in T_{REC}. The dashed line shows the theoretical decrease of standard error for a completely stable case, calculated by fitting a $n^{-1/2}$ curve to the initial part of the standard error curve.

diometric resolution is the theoretical value of the standard error for an averaging length of just one sample, which is undefined. That value is equivalent to the standard deviation of the sample values when only white noise is present. In order to obtain the ΔT_N from flight data, a curve of the form $n^{-1/2}$ is fitted to the initial part of the standard error curve for averaging length n. An example of such a plot is shown in Fig. 9, for channel 17's views of the ambient target during a period of flight where the target was warming. For this particular example, smoothing the data with an averaging time greater than about 34 s begins to reduce the resultant accuracy, attenuating the nonrandom components of the signal.

Low frequencies in the radiometer output are dominated by $1/f$ noise, due to instabilities in the amplifiers, as discussed in Saunders et al. (1995). Averaging calibration data over a period can improve the accuracy of T_{REC} by minimizing the white noise; this is equivalent to increasing the radiometer's integration time for the target views. The maximum period over which these data can be averaged while improving the accuracy of the mean is limited by the $1/f$ knee frequency. The knee frequency represents the frequency at which $1/f$ noise starts to dominate over the white noise and can be estimated from plots such as Fig. 9. Typically for MARSS, averaging 10 consecutive calibration views (30 s) reduces the uncertainty in T_{REC} by a factor of 2.5. Table 3 also shows the corresponding averaging period for minimum standard error, derived from a large amount of flight data over a range of conditions. A correlation is noted between the optimum averaging length and the receiver noise, as averaging length considerations are dominated by the same fluctuations of the target temperatures for all channels, with each channel's receiver noise added to that. Observations have also noted that channel 17's T_{REC} is more variable than that of the other channels, and this is reflected in a shorter optimum averaging length than might be expected simply from the ΔT_N.

The noise power spectrum of MARSS's gain can be analyzed in the same way. In this case, the $1/f$ noise is due to temperature induced gain change in the 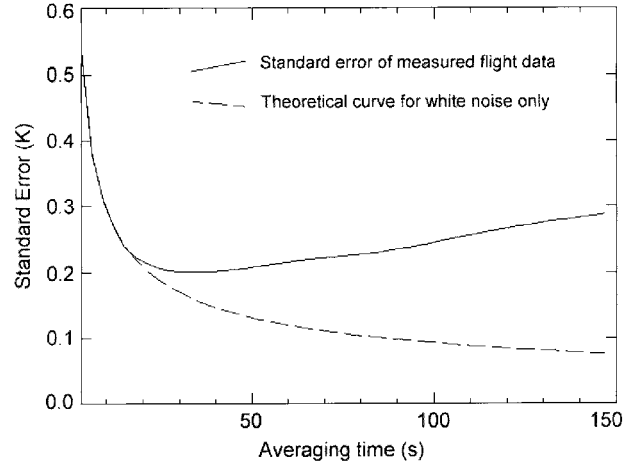IF amplifiers. Since these are under active thermal control, the calibration data can be averaged over a much longer period for the gain than for T_{REC}. The standard error of gain in stable flight conditions simply follows the $n^{-1/2}$ form, indicating that the accuracy of the gain continues to improve when the averaging period is extended to tens of minutes. Unstable flight conditions (temperature changing) shorten the optimum smoothing period, and an averaging length of 10 min was selected as a suitable value for normal flight data. This reduces the uncertainty in the gain by more than a factor of 10, to 0.1%. Without such smoothing, higher-frequency noise would dominate the error budget when extrapolating the calibration to low brightness temperatures.

Radiometer stability under varying pressure was also investigated using the thermal vacuum chamber. These investigations verified the expected pressure independence of MARSS, with the radiometer's calibration remaining stable and unchanged at different pressures between 300 and 1000 hPa.

6. Resultant errors in retrieved brightness temperatures

Table 4 shows error sources expressed in kelvins and the effects of each of these when propagated independently through the radiometer equations (1)–(3) to retrieve brightness temperatures. This analysis assumes an ambient target temperature of 253 K, a hot target temperature of 333 K, and an observed scene of 3 K. Scenes closer to the ambient temperatures will have proportionally smaller errors. Radiometer noise is lower for the target views than the scene because of the longer integration time available, the scene errors quoted being for a single uncorrelated measurement. Averaging consecutive views of a homogeneous scene would reduce

TABLE 4. Error contributors expressed in K. ''Hot'' and ''ambient'' refer to figures for the heated and ambient calibration targets, respectively, while ''scene'' is the uncertainty in radiance of a single observation. Here, ϵT_B is the uncertainty in the retrieved brightness temperatures calculated by propagating these contributors independently through the radiometer equations (1)–(3). ''Total uncertainty'' is an average of the combined error contributors (random and bias) for a single view of a low brightness scene.

Source of error	Type	Hot	Ambient	Scene	ϵT_B
Nominal values		333	253	3	
Mirror reflectivity	Bias			0.27	0.27
PRT calibration	Bias	0.05	0.05		0.26
Target gradient	Bias	0.20			0.63
Target stability	Random	0.03	0.05		0.05
Channel 16 noise	Random	0.15	0.15	0.46	0.49
Channel 17 noise	Random	0.32	0.32	0.72	0.80
Channel 18 noise	Random	0.20	0.20	0.62	0.65
Channel 19 noise	Random	0.13	0.13	0.42	0.44
Channel 20 noise	Random	0.10	0.10	0.33	0.35
Channel 16 resultant	Total uncertainty for a single obser-				0.88
Channel 17 resultant	vation of 3-K scene (rms)				1.09
Channel 18 resultant					0.98
Channel 19 resultant					0.86
Channel 20 resultant					0.81

the contribution of random fluctuations, although uncertainties due to biases cannot be so reduced.

7. Conclusions

The Met Office undertook a thorough characterization of the MARSS system using the Defence Evaluation and Research Agency thermal-vacuum test facility and flight trials. A high system accuracy was obtained by investigation of separate error sources. Effects such as the scan dependence introduced by reflectivity variations of the scan mirror to varying angle of incident polarization can be accurately modeled but must be considered to achieve high accuracy. Knowledge of the stability of various calibration parameters allows data smoothing to minimize noise and random errors to the point where uncertainty in the temperature of the system's calibration targets is the dominant source of error. Resultant system accuracy for all channels except channel 16 is found to be approximately 1 K. At the time of the thermal-vacuum chamber tests, channel 16 was

suffering from an RFI contamination causing a substantial and variable nonlinearity; however, following corrective action further flight trials and ground tests suggest that it now matches the other channels' performance.

REFERENCES

English, S. J., 1995: Airborne radiometric observations of cloud liquid-water emission at 89 and 157 GHz: Application to retrieval of liquid-water path. *Quart. J. Roy. Meteor. Soc.,* **121,** 1501–1524.
——, C. Guillou, C. Prigent, and D. C. Jones, 1994: Aircraft measurements of water vapour continuum absorption. *Quart. J. Roy. Meteor. Soc.,* **120,** 603–625.
Guillou, C., S. J. English, C. Prigent, and D. C. Jones, 1996: Passive microwave airborne measurement of the sea surface response at 89 and 157 GHz. *J. Geophys. Res.,* **101** (C2), 3775–3788.
Han, Y., and E. R. Westwater, 2000: Analysis and improvement of tipping calibration for ground-based microwave radiometers. *IEEE Trans. Geosci. Remote Sens.,* **38,** 1260–1276.
Hewison, T. J., 1991: Reflectivity tests of microwave black body targets. Met Office Remote Sensing Branch Working Paper No. 27, 22 pp. [Available from Head of Remote Sensing Branch, Met Office, Y70 DERA, Farnborough, Hants GU14 0LX, United Kingdom.]
——, 2001: Airborne Measurements of Forest and Agricultural Land Surface Emissivity at Millimetre Wavelengths. *IEEE Trans. Geosci. Remote Sens.,* **39,** 393–400.
——, and S. J. English, 1999: Airborne retrievals of snow and ice surface emissivity at millimetre wavelengths. *IEEE Trans. Geosci. Remote Sens.,* **37,** 1871–1879.
Jones, D. C., 1995: Validation of scattering microwave radiative transfer models using an aircraft radiometer and ground-based radar. Ph.D. thesis, University of Reading, 205 pp.
McGrath, A. J., 2000: MARSS Thermometry Characterisation. Met Office Remote Sensing Branch Working Paper No. 178, 20 pp. [Available from Head of Remote Sensing Branch, Met Office, Y70 DERA, Farnborough, Hants GU14 0LX, United Kingdom.]
Morland, J. C., D. I. F. Grimes, G. Dugdale, and T. J. Hewison, 2000: The estimation of land surface emissivities at 24 to 157 GHz using remotely sensed aircraft data. *Remote Sens. Environ.,* **73,** 323–336.
Saunders, R. W., T. J. Hewison, S. J. Stringer, and N. C. Atkinson, 1995: The radiometric characterization of AMSU-B. *IEEE Trans. Microwave Theory Tech.,* **43,** 760–771.
Ström, J., R. Busen, M. Quante, B. Guillemet, P. R. A. Brown, and J. Heintzenberg, 1994: Pre-EUCREX intercomparison of airborne humidity measuring instruments. *J. Atmos. Oceanic Technol.,* **11,** 1392–1399.
Vinogradov, E. A., E. M. Dianov, and N. A. Irisova, 1967: Dielectric characteristics of liquid nitrogen at lambda = 2.3 mm. *Sov. Phys. Tech. Phys.,* **11,** 983.